

Transition between quantum confinement and bulklike behavior in polar quantum wellsLukas Uhlig^{1,*}, Jannina Tapaß¹, Mateusz Hajdel², Grzegorz Muziol² and Ulrich T. Schwarz¹¹*Institute of Physics, Chemnitz University of Technology, 09126 Chemnitz, Germany*²*Institute of High Pressure Physics, Polish Academy of Sciences, 01-142 Warsaw, Poland*

(Received 13 April 2023; revised 9 June 2023; accepted 14 June 2023; published 7 July 2023)

The properties of III-nitride quantum wells (QWs) are significantly affected by polarization fields. We show that, in the case of wide QWs, there exist two fundamentally different transition types characterized by quantum-confinement effects or bulklike behavior—depending on the carrier density in the structure. At low carrier density, spontaneous and piezoelectric polarization lead to tight confinement and low spatial overlap between the electron and hole wave functions. However, if the carrier density is sufficient for screening of the polarization fields, the wave functions spread out, reach high overlap, and the energy states come close to each other, similar to a bulk semiconductor. Streak camera measurements in the subthreshold regime of nitride laser diodes and numerical simulations show consistent results and let us clearly differentiate between contributions of individual states for low carrier density and the emergence of a high density of energetically close states at high carrier density.

DOI: [10.1103/PhysRevB.108.045304](https://doi.org/10.1103/PhysRevB.108.045304)**I. INTRODUCTION**

Quantum wells (QWs) are one of the core technologies in recent optoelectronics and electronics, as they usually form the active region of light-emitting diodes and laser diodes and are applied in transistors, absorbers, and photodetectors [1–4]. Charge carriers are confined in a few-nanometer-thin layer, because the band-gap energy is smaller than in the surrounding barrier layers. Thus, high spatial overlap between electrons and holes can be obtained, which is needed for highly efficient devices. As a consequence of the spatial confinement in one dimension, a two-dimensional electron gas with discrete energy levels is formed. These energy states depend on the thickness of the QW, similar to the well-known particle in a box [3].

Wide QWs in the GaN/InGaN material system have gained much attention due to their unexpected efficiency and potential. The quantum-confined Stark effect (QCSE) describes the decreased transition energy and spatial overlap of electron and hole wave functions due to a built-in electric field in the QW that results from spontaneous and piezoelectric polarization [5–12]. The electric field pulls electrons and holes towards the opposite ends of the QW and this effect is even more pronounced in thicker QWs [9,12]. This would suggest very ineffective devices when going beyond the usual thickness of 2–3 nm, but surprisingly efficient LEDs and laser diodes have been demonstrated with up to 25-nm-wide QWs [13–17]. The

reasons for the high efficiency of wide QWs are the screening of the electric field due to high carrier density as well as the involvement of excited states, leading to a high wave-function overlap. In various papers [16–22], experimental evidence for transitions between excited states has been reported and simulations of wide QWs with screened electric field show high overlap of the first excited states ($e_2 h_2$), but even higher states have rarely been considered. In asymmetric QWs, the selection rules are relaxed, allowing all transitions between sublevels with their strength depending on the screening of the field. Many people disagree with the term “quantum well” for 25-nm-thick layers for obvious reasons. The Bohr radius for excitons, often regarded as a yardstick of quantum confinement, is only 3 nm for GaN. Even for conventional III-V semiconductors with a higher Bohr radius, a 25-nm-thick layer is considered a heterostructure rather than a QW. However, in this paper we stick to this term, as we still observe typical QW-like behavior, depending on the operation conditions.

As a model system, we use blue InGaN laser diodes, driven below the laser threshold. Here we identify two operation regimes in experiments and numerical simulations, showing consistent results: In the case of low carrier density, electrons and holes are found in narrow triangular potentials at both sides of the QW, which is similar to typical quantum confinement but electrons and holes are spatially separated. For high carrier density, the electric field becomes screened and several excited states are responsible for stronger emission. Especially for a 25-nm-wide QW, the structure resembles more a bulk layer with almost rectangular potential profile and, consequently, a large number of states become active, whose energy spacing is smaller than homogeneous and inhomogeneous broadening.

The fundamental difference between a 2D and 3D electron gas is in the density of states: in a 2D system there are separated energy levels and each one contributes a fixed

*lukas.uhlig@physik.tu-chemnitz.de

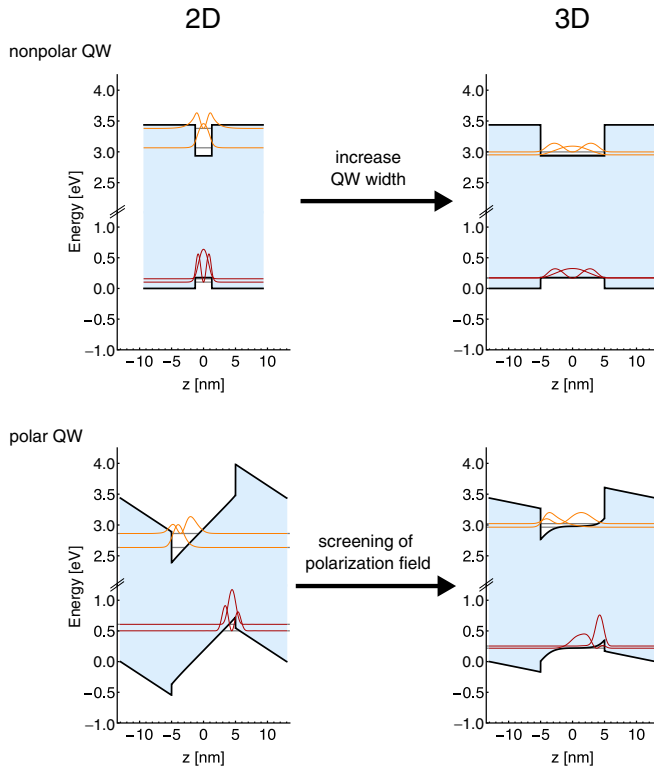


FIG. 1. Traditionally, the thickness of a layer defines its function either as a quantum well (2D electron gas) or bulklike heterostructure (3D electron gas). Polar QWs offer another degree of freedom, which is the charge carrier density in the QW, partly screening the polarization field. This determines the potential shape and thus the density of electronic states as well as the spatial overlap between electron and hole wave functions. Numerical simulations of nonpolar or polar InGaN QWs illustrate the two- or three-dimensional character of the system as a function of thickness or carrier density. For no involved polarization field, the QW thickness variation from 2.6 nm to 10.4 nm clearly changes its character. In case of a 10.4-nm-wide polar QW, a similar effect is obtained by increasing the carrier density from 10^{12} cm^{-2} to 10^{13} cm^{-2} . The three lowest states of electrons (orange) and heavy holes (red) are plotted.

amount of states, so the total density of states $D_{2D}(E)$ shows steps at each energy level and is constant in between. In a 3D electron gas, the density of states is proportional to the square root of the energy, $D_{3D}(E) \sim \sqrt{E}$. In the transition regime between 2D and 3D, the energy separation between the QW states becomes smaller until it is effectively a continuum of states, following the 3D dispersion relation [23]. In previous works, this 2D-3D transition has been observed as shifting energy states in different samples with varied QW thickness in the AlGaAs/GaAs or GaN/InGaN material systems [24–26].

In our experiments, we can see such 2D- or 3D-like behavior in the same device, which is unique to polar heterostructures. The transition between these two regimes depends on the charge carrier density, which is illustrated in Fig. 1 using our numerical simulation model. Furthermore, we measure time-dependent switching from the quantum-confinement to bulk character as the carrier density rises after the current has been switched on.

II. TIME- AND CURRENT-DEPENDENT SPECTRAL TRANSITION

We investigate edge-emitting InGaN Fabry-Pérot laser diodes grown by plasma-assisted molecular beam epitaxy [27], where the active region is formed by a single $\text{In}_{0.17}\text{Ga}_{0.83}\text{N}$ QW with a thickness of either 10.4 nm or 25 nm. A cavity length of $1000 \mu\text{m}$ and a ridge width of $3 \mu\text{m}$ is used. Further details of the device structure can be found in Appendix A. The packaged devices are electrically driven with 80-ns-long current pulses using a low duty cycle of 10^{-3} . The emitted light is collimated and coupled into a monochromator that is attached to a streak camera (see Appendix B for more details). In this way, we measure the time-resolved emission spectra depending on driving current density. To observe the influence of charge carrier density on the internal electric fields and electronic states, the laser diode is operated below threshold to avoid clamping of the carrier density. Figure 2 shows the emission behavior for the 10.4-nm-thick QW. The optical response is shorter than the driving pulse because of low injection rate. The emission starts only after a sufficient density of carriers has been injected into the QW, which partially screen the polarization field. After that, the subsequently supplied carriers can give rise to luminescence. As can be seen, the time required for screening the electric field is smaller for a higher injection rate (higher current density). Furthermore, in the low-current regime, we observe spectral broadening towards longer wavelengths and a new dominant peak at 470 nm, which is illustrated in Fig. 2(e). Also note the stable short-wavelength edge of the spectrum at 450 nm, where the blue-shift is saturated.

For the device with a 25-nm-thick QW, there is also a current-dependent transition in the spectrum, as shown in Fig. 3. At the lowest current density, we measure a broad spectrum with 475-nm peak wavelength, which significantly extends to long wavelengths. At higher currents, the main peak around 458 nm arises. These two spectral contributions also have very different strengths and time-dependent behaviors. Below 0.3 kA cm^{-2} , the broad peak is very weak compared to the main peak and starts less than 20 ns after onset of the electrical signal. In contrast, at 0.4 kA cm^{-2} a stronger, narrower emission peak is found that starts later, about 60 ns after the current pulse. The weak and broad emission actually forms a background signal, which is also present at currents of 0.4 kA cm^{-2} and higher, but cannot be detected next to the strong main peak due to the huge intensity difference.

To investigate this transition in more detail, the streak camera image from Fig. 3(c) is plotted in Fig. 4 using a logarithmic color scale. After a long delay of 40 ns, the peak at 470 nm gains intensity first, but then another emission peak at 455 nm becomes active and we see a dynamical spectral transition from the 470 nm to the 455 nm peak happening on a time scale of about 10 ns. This is illustrated by the spectra in Fig. 4(b) and the intensity of both peaks as function of time in Fig. 4(c). These observations show that the occurrence of both peaks is not only related to the pulse current but is rather dependent on the carrier density, which has not yet reached its equilibrium value after 50 ns due to the low current of 0.4 kA cm^{-2} . At some point, the carrier density is

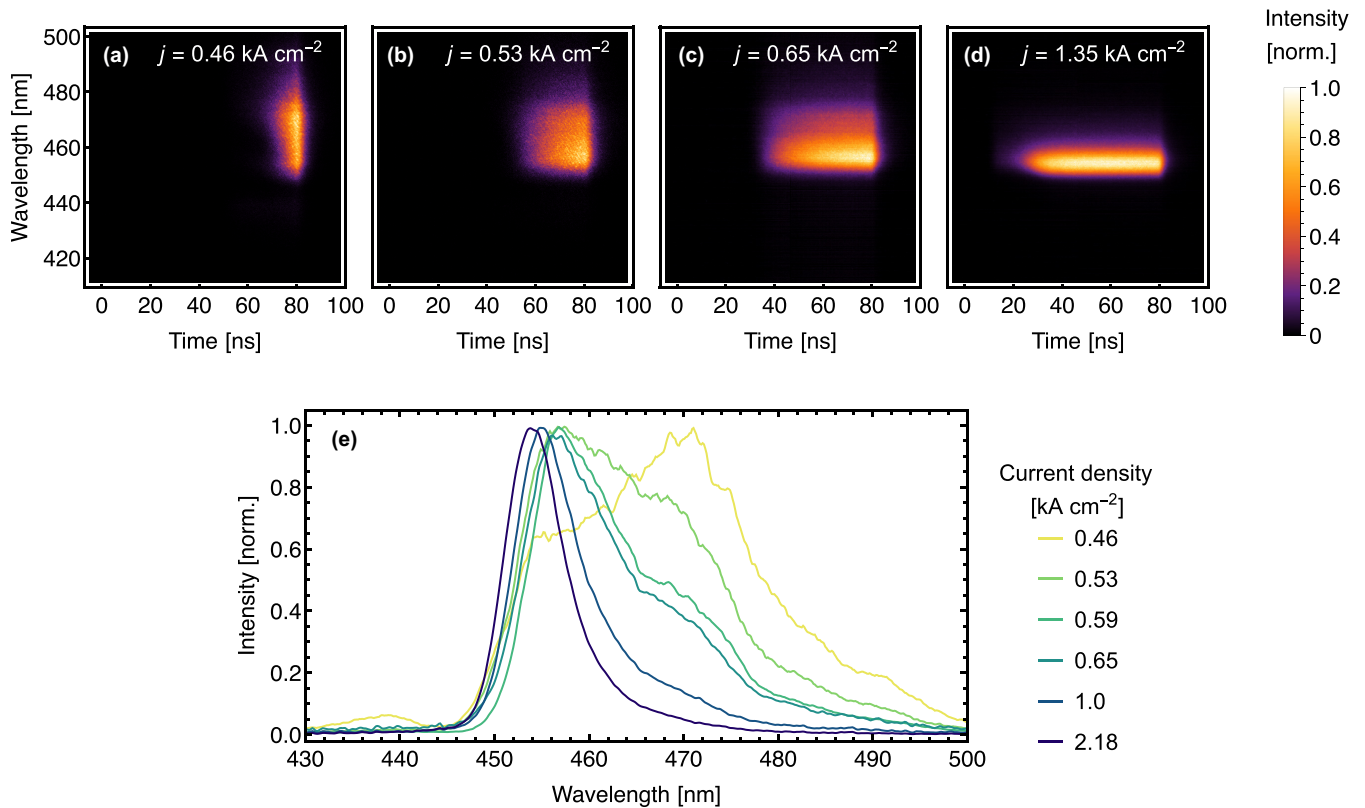


FIG. 2. Streak camera measurements on the 10.4-nm-thick QW. (a)–(d) Spectral-temporal dynamics and (e) time-integrated spectra for different pulse currents. The 80-ns-long driving pulse starts at $t = 0$ ns. Images (a) and (b) have been measured using photon counting and (c) and (d) in analog integration mode.

sufficient for effective recombination at 470 nm and shortly afterwards, the even stronger transition at 455 nm becomes active.

Now, how can we understand this unusual behavior of below-threshold emission in wide-well laser diodes? Conventional devices with a QW thickness of 2–3 nm usually exhibit only one peak featuring a moderate blue-shift for increasing current [21]. This corresponds to the ground-state transition $e_1 \rightarrow h_1$ and excited states are not involved here, because of their vanishing population due to the large energy difference between ground and excited states in thin QWs. As an example, $\Delta E_{hh_1-hh_2} \approx 70$ meV, $\Delta E_{e_1-e_2} \approx 300$ meV $\gg k_B T \approx 26$ meV for a 2.6-nm-wide QW, whereas transitions to heavy and light holes of the same subband with $\Delta E_{hh_1-lh_1} \approx 10$ meV cannot be distinguished due to inhomogeneous broadening. The transition energy is influenced by the charge carrier density inside the QW as follows: After a short time (few ns to tens of ns), the carrier density has established a current-dependent equilibrium value, which is higher for higher current. High carrier density leads to (i) band filling, where increased quasi-Fermi-level splitting causes a higher population with energetically higher carriers, and (ii) screening the electrical field across the QW, which weakens the QCSE. Both effects cause the transition energy to increase if the carrier density becomes higher.

In the case of wide QWs, it is expected that the wave functions of electron and hole ground states have negligible spatial overlap because the tilted potential landscape leads to localization of the ground states at the opposite ends of the QW. So,

only transitions between excited states of electrons and holes can reach substantial overlap and contribute to spontaneous emission and gain. For this, it is also necessary to screen the internal field at least partially by a sufficient carrier density in the QW. Thus, we attribute the weak long-wavelength emission that we measure at lowest current to weak screening, where the transition energy is reduced due to the QCSE and the small spatial overlap of electron and hole wave functions causes the low intensity. In this case, recombination is usually governed by the ground state, because higher states are practically not populated. At higher currents, carrier injection is faster and if the critical carrier density for effective screening is reached and the excited states are sufficiently populated, the new transition quickly causes bright emission at shorter wavelength. The observed saturation of the blue-shift indicates complete screening, where the transition energy approaches the InGaN band-gap energy. The delay after the start of the electrical pulse until the sufficient carrier density is reached depends on the applied current, as our measurements show. Not only the injection rate (i.e., current) but also the initial carrier density at the beginning of the pulse determines this delay, similar to the turn-on delay for lasing [28]. Previous studies showed that so-called dark carriers can survive for unusual long times in wide QWs if the internal fields are not screened and all radiative and nonradiative recombination processes are prevented by very low wave-function overlap [16,20,29,30].

We would like to better understand the measured transition dynamics in wide QWs regarding the involved states, their population, and the nature of both operation regimes,

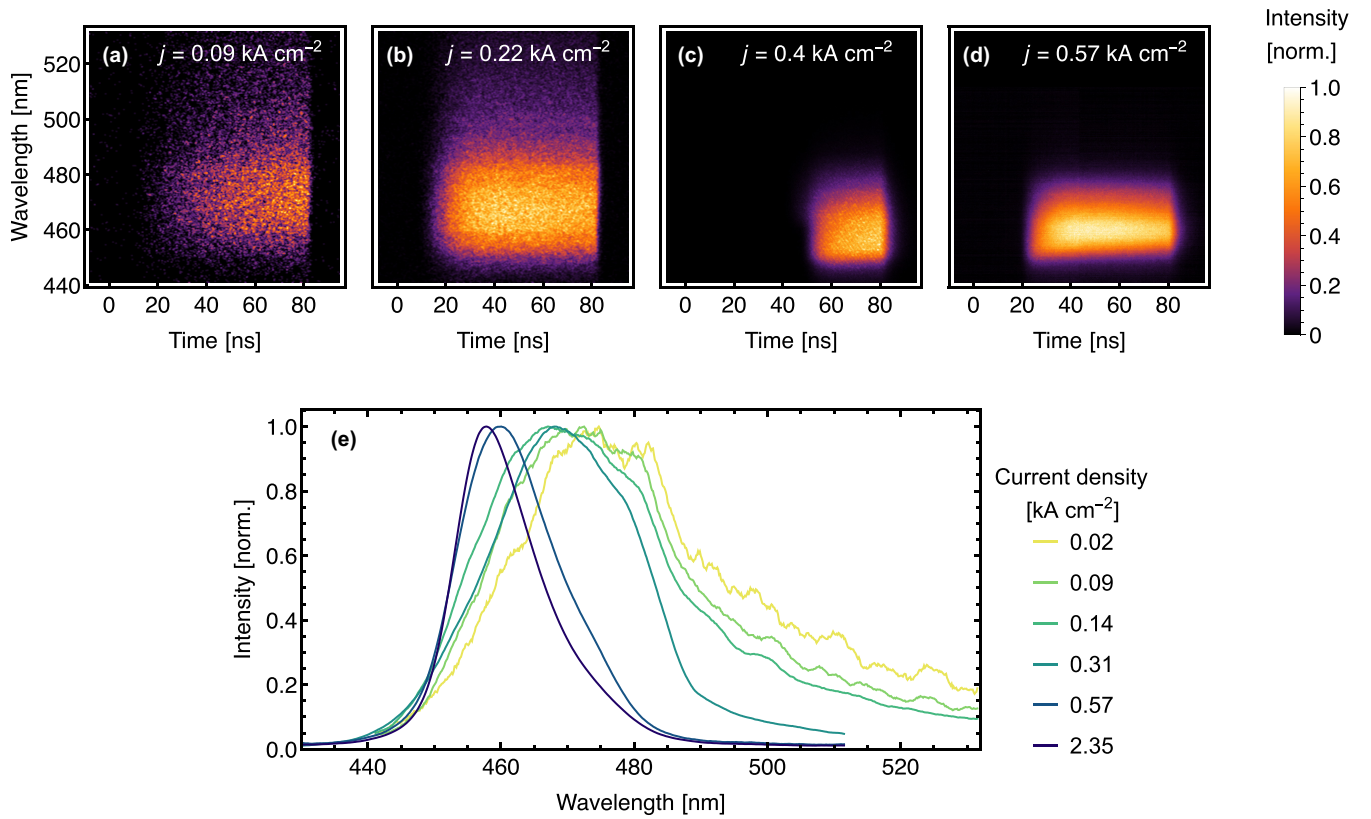


FIG. 3. Streak camera measurements on the 25-nm-thick QW. (a)–(d) Spectral-temporal dynamics and (e) time-integrated spectra for different pulse currents. The 80-ns-long driving pulse starts at $t = 0$ ns. Images (a) and (b) have been measured using photon counting and (c) and (d) in analog integration mode.

so we decided to study these effects using numerical simulations.

III. SIMULATION OF ELECTRONIC STATES DURING CARRIER-DEPENDENT TRANSITION

We calculate the energies of the confined electronic states in the QW as well as their transition matrix elements and spontaneous emission rate by using established models for solving the Poisson and Schrödinger equations [31–33] using the physical parameters from [34]. The approach is described in Appendix C.

With the help of these calculations, we can directly observe how the shape of the potential, energy states, and wave functions are affected by the carrier density. Figure 1 illustrates the situation for 10.4-nm-wide QWs. Detailed plots depicting different carrier densities in 10.4-nm- and 25-nm-wide QWs can be found in Appendix D. In the case of a very low carrier density of $N = 10^{12} \text{ cm}^{-2}$, the potential is practically unscreened and the triangular shape leads to confinement of the electron and hole wave functions in small regions on the opposite sides of the QW. Consequently, the energy differences between ground and excited states in the same band are relatively large. Thus, the population of excited states is

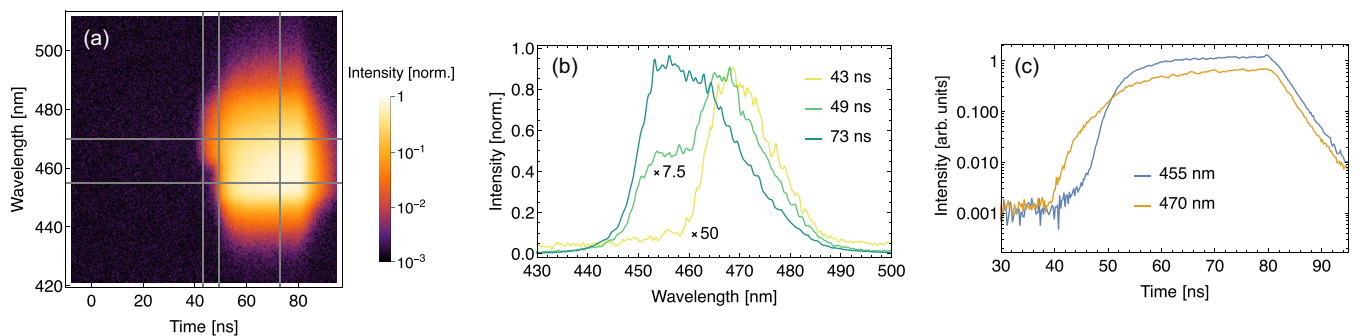


FIG. 4. Time-dependent spectral transition in the 25-nm-thick QW. (a) Streak camera image for a current density of 0.4 kA cm^{-2} plotted using a logarithmic color scale, (b) spectra taken at different times in the pulse: 43 ns, 49 ns, and 73 ns, (c) logarithmic intensity curves of the emission at 455 nm and 470 nm over time.

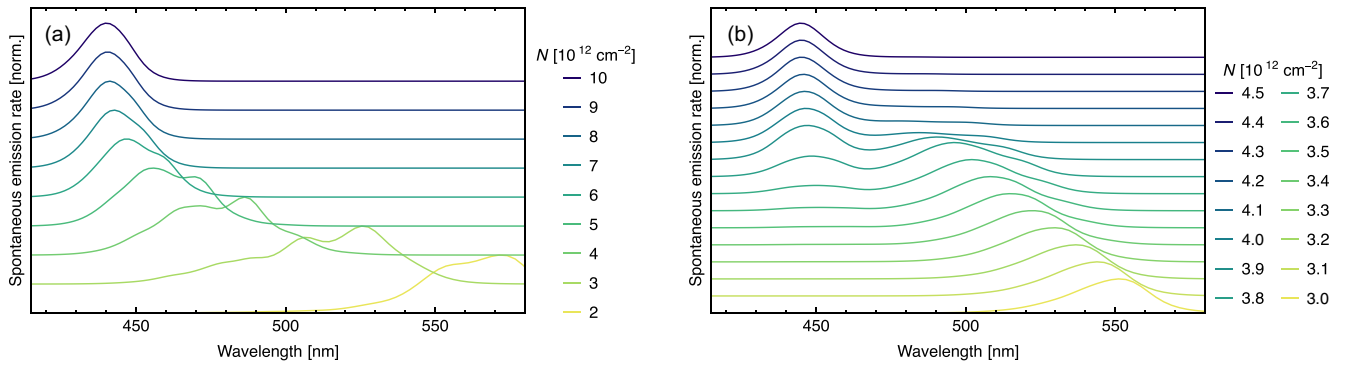


FIG. 5. Calculated spontaneous emission spectra in (a) 10.4-nm- and (b) 25-nm-wide QWs for different carrier densities.

very low and the ground states of electrons and holes have almost zero spatial overlap, which makes recombination very unlikely. If the carrier density now becomes higher, the charge distribution significantly impacts the potential landscape by screening the polarization field. The QW potential becomes more rectangular, the wave functions spread out more, and a substantial overlap is reached, especially for the excited states. In this case, the ground states are still spatially separated and have the highest population, so they are mainly responsible for screening the field. With a smaller electric field in the QW, the charge carriers effectively occupy a larger region and quantum confinement gets weaker, which we observe as smaller energy separation between states of the same band. Especially for the very wide 25-nm QW and high carrier density, the states in each band come very close to each other and appear more as a continuum than as separate confined states. In this case, the QW rather acts as a heterostructure than as a two-dimensional system.

We calculate the spontaneous emission spectra and compare them to our measurements. The simulated spectra from the 10.4-nm-wide QW are plotted in Fig. 5(a) and show long-wavelength emission as well as multiple peaks at low carrier densities. The transition energies depend on the carrier density as expected (see also Fig. 1) due to screening of the built-in electric field. For high carrier densities, one main peak emerges at around 440 nm and stays present also at carrier densities above 10^{13} cm^{-2} (not shown), where the normalized spectrum stays approximately constant and the wavelength-shift has saturated. At this point, the electric field is maximally screened.

We can only make qualitative comparisons to the experimental data because the carrier density cannot be measured directly. However, the spectral effects in the experiment (see Fig. 2) and in the simulations agree well. Experimentally, at low carrier density (at $j = 0.5 \text{ kA cm}^{-2}$) we observe a peak at 470 nm and a side peak towards shorter wavelength, resembling the calculated spectrum at $N = 5 \times 10^{12} \text{ cm}^{-2}$. At higher carrier densities, the peak on the shorter wavelength side becomes stronger, eventually dominates the emission and exhibits a slight blue-shift with increasing current or carrier density. The current density of 1 kA cm^{-2} roughly corresponds to a carrier density of $8 \times 10^{12} \text{ cm}^{-2}$, which is the point from where the normalized spectrum stays mainly constant and the polarization field is mostly screened. In the simulations we can also investigate the carrier density range

below $5 \times 10^{12} \text{ cm}^{-2}$ down to the completely unscreened case, but in this range the intensity becomes extremely low due to the vanishing wave-function overlap. At some point, the sensitivity of our experiment is the limiting factor. However, for the almost unscreened potential, the carrier lifetime becomes very long. Dark carriers have been observed up to 3 ms after optical excitation [30], so very low emission is expected in this situation.

The calculated spectra for the 25-nm-wide QW are shown in Fig. 5(b) and similarly to the 10.4-nm QW [see Fig. 5(a)], a stable main peak in the high-carrier regime is present as well as additional low-energy contributions for lower carrier densities. Note that in Fig. 5(b) a smaller range in N is chosen to illustrate the most interesting part of the transition. For even smaller carrier densities, the red shift is further continued, whereas for higher densities the single peak at 445 nm stays stable. Here we see a clear transition between two operation regimes, which are:

- (1) (for low N) the broader emission at longer wavelengths featuring a strong dependency on carrier density;
- (2) (for high N) the stable peak at shorter wavelengths that barely depends on carrier density.

The corresponding measurements in Fig. 3 show an abrupt transition between these two conditions, which is reflected in the calculations by strong spectral changes for small steps in the carrier density. There are some deviations in the shape of the spectra between experiment and simulation, however, the general behavior is well comparable.

We attribute these two situations to the quantum confinement and bulklike behavior, which becomes more clear if we have a look at the density of states as well as the individual transitions that contribute to the spectra. The density of states as a function of energy in both conduction and valence bands reflects the nature of carrier confinement. Figure 6 depicts the situation in 10.4-nm- and 25-nm-wide QWs. The effective band-gap energy increases for higher carrier densities until it saturates, approaching the bulk band-gap energy of $\text{In}_{0.17}\text{Ga}_{0.83}\text{N}$, which is 2.76 eV. This means that both the 10.4-nm- and 25-nm-wide QWs are almost completely screened at a carrier density of 10^{13} cm^{-2} . However, the QW thickness still has profound implications on the distribution of the density of states as function of energy. For a very low carrier density ($N = 10^{12} \text{ cm}^{-2}$), the density of states is characterized by steplike behavior in both conduction and valence bands, for both considered QW thicknesses. In case of

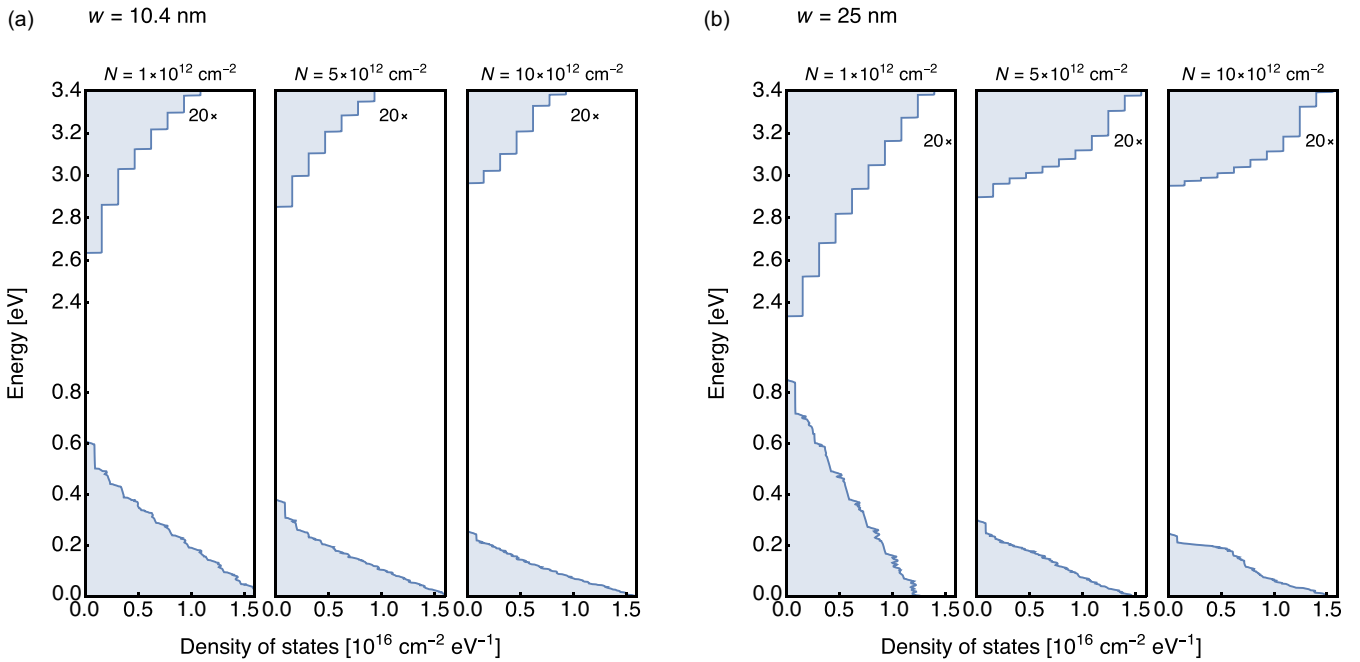


FIG. 6. Calculated density of states in conduction and valence bands of a (a) 10.4-nm- or (b) 25-nm-wide QW. The situation is plotted for three different charge carrier densities from 10^{12} cm^{-2} to 10^{13} cm^{-2} .

the 10.4-nm-wide QW, for rising carrier density, the electron levels shift towards higher energy, while in the valence band the steps in the density of states already start to disappear. This is due to the larger effective mass of holes, leading to closely spaced valence band states. In case of the 25-nm-wide QW, the energy shift of electron and hole states is substantially larger and for increasing carrier density, the conduction band also approaches a smooth density of states with very close steps. The envelope of the density of states is characteristic for the varying shape of the confining potential. A (thin) QW with rectangular potential (i.e., without polarization fields) would have an envelope to their steplike density of states that approaches the three-dimensional limit $D_{3D}(E) \sim E^{\frac{1}{2}}$. In contrast, in the low-carrier regime our calculations rather show a linear or superlinear envelope $D(E) \sim E^p$ with $p \geq 1$. This signifies the distorted potential shape and is, in general, similar for both conduction and valence bands, only the valence band is additionally influenced by crystal-field split-off bands that appear around 0.1 eV. In a triangular potential, the energy separation between states becomes smaller with higher energy because the width of the potential well increases accordingly. This means we can follow the changing character of carrier confinement not only in the apparent potential shape (see Fig. 1) but also reflected in the density of states.

Figure 7 illustrates the contributions of all the different transitions in the calculated spontaneous emission spectra of 10.4-nm- and 25-nm-wide QWs. Each transition from a certain conduction band state e_i to a valence band state h_j leads to a continuous contribution obtained by integration over k_x and convolution with a hyperbolic secant function to account for homogeneous broadening. The sum over all transitions makes up the emission spectrum R_{sp} . Here we take the product of the squared transition matrix element and electron and hole population probabilities $|M_{ij}(k_x)|^2 f_c(E_{c,i}(k_x)) [1 - f_v(E_{v,j}(k_x))]$ at

the Γ point ($k_x = 0$) as a measure of how strong the transition $e_i \rightarrow h_j$ is involved in emission. The transitions are marked according to the involved conduction band state e_i as the corresponding hole states h_j are closer to each other and they can be identified by their energetic order. The spectral peak that corresponds to each transition appears slightly blue-shifted compared to the respective transition energy. This is because of band filling and contribution of $k \neq 0$ states, i.e., the transition energy forms the onset of available states, but most occupied states are higher in energy. In the 10.4-nm-wide QW, at very low carrier density [see Fig. 7(a)], only the electron ground state contributes to light emission and the $e_1 \rightarrow h_1$ transition is the strongest. For increasing carrier density [e.g., $4 \times 10^{12} \text{ cm}^{-2}$ in Fig. 7(e)], we observe three partly merged spectral peaks, which can be attributed to the first three electron states and, for all of them, multiple hole states take part in the emission. Due to the Fermi-Dirac distribution, the lower-energy transitions are weighted stronger, even though their wave-function overlap is lower than in other transitions. For an even higher carrier density, the QW potential changes its shape and the electron states shift higher in energy and come closer together. The three peaks merge and the state e_2 dominates over the other electron states [see Fig. 7(i)].

In the 25-nm-thick QW, there are two peaks originating from few transitions in the low-energy regime, involving almost only e_1 . This corresponds to the usual behavior of confined states in a QW, where characteristic transitions form the spectrum by having high population and sufficient overlap. However, at sufficiently high carrier densities, emission in the high-energy part of the spectrum originates from the high joint density of states, comparable to a band in a bulk semiconductor. This contribution becomes stronger because of increasing screening of the electrical field by higher carrier densities, which causes the energy states to come closer

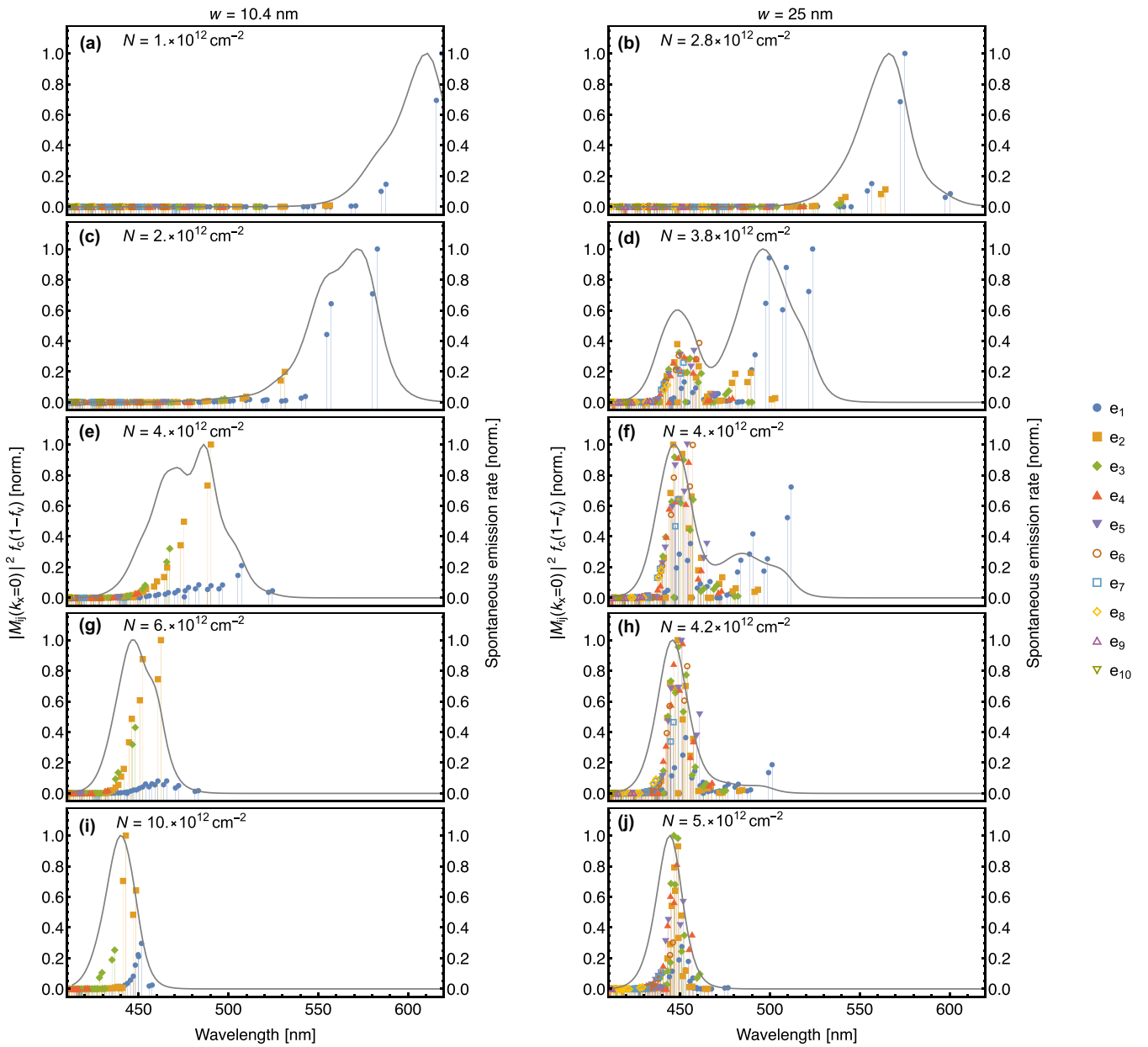


FIG. 7. Spontaneous emission spectra and the corresponding transitions in 10.4-nm- and 25-nm-wide QWs. The contributions of the ten energetically lowest electron states are marked with different colors. The different points of one color represent the involved hole states.

together and also the wave-function overlap increases substantially. In comparison with the screened 10.4-nm-wide QW, the broader extended wave functions in the screened 25-nm-wide QW cause even smaller energy differences between higher states, which leads to high population of much more states simultaneously, approaching a continuum of states. For the screened 25-nm-wide QW [see Fig. 7(j)], transitions involving the electron confined states e_1 to e_7 lie within an energy range of 100 meV, while for the 10.4-nm-wide QW [see Fig. 7(i)] only the first three lowest electron confined states lie within such an energy range. This corresponds to the nearly bulklike conduction band density of states for the 25-nm-QW, while for the 10.4-nm QW even at highest carrier densities only a small number of confined states contribute to the density of states (see Fig. 6) due to the narrower quantum confinement.

Note that all the simulated spontaneous emission spectra are calculated without inhomogeneous broadening, which allows us to relate the subpeaks in Fig. 7 to important transitions. With the inclusion of inhomogeneous broadening, the calculated spectra could be closer to the measurements [35].

IV. CONCLUSIONS

In this paper, we investigated two different operation regimes of wide InGaN QWs, defined by quantum confinement and bulklike behavior, as well as the transition between both regimes. When the device is operated at very low current, the active region is populated with a low charge carrier density and the spontaneous and piezoelectric polarization lead to a triangular potential landscape in the QW. Especially

in wide QWs, the electric fields play an even stronger role as the ground states of electrons and holes are confined at opposite ends of the QW, and have very low wave function overlap and a low transition energy. If a sufficiently high carrier density is reached, the system shows rather a bulklike behavior, where the fields are screened and the wave functions of excited states extend over the whole width of the structure. The energy states in each band come very close to each other (in the range of the homogeneous linewidth) and rather start to form a steady density of states, especially in the 25-nm-wide QW. This transition, which depends on carrier density, will be present only in polar semiconductors such as III-nitrides and is not observed in conventional III-V semiconductors.

We investigated this behavior experimentally in laser diodes with wide QWs as current-dependent changes in the emission properties but also as dynamical switching in time-dependent streak camera measurements. Numerical simulations are able to reproduce these effects and help us obtain deeper insights on which states are involved in each operation regime. Our observations are not exclusive to laser diodes, but apply to LEDs or similar devices with wide polar QWs as well. In the simulations, only the QW and barrier layers are taken into account, which means that this minimalistic model can be arbitrarily expanded to complete devices, while the essential effects are already included in the simple case that we consider in this paper.

ACKNOWLEDGMENT

This work was supported partially by National Science Centre Poland Grants No. 2019/35/D/ST3/03008 and No. 2019/35/N/ST7/02968.

APPENDIX A: DEVICE STRUCTURE

The epitaxial structure for the edge-emitting laser diode is grown on a *c*-plane Ammono GaN substrate using plasma-assisted molecular beam epitaxy. The silicon-doped *n*-side cladding consists of a 50-nm GaN layer, a 700-nm Al_{0.065}Ga_{0.935}N layer, and a 100-nm GaN layer. This is followed by the undoped waveguide layers, containing an In_{0.17}Ga_{0.83}N QW surrounded by two 110-nm-thick In_{0.04}Ga_{0.96}N waveguiding layers. On the *p* side, a 20-nm-wide Mg-doped Al_{0.13}Ga_{0.87}N electron blocking layer is grown. The second cladding consists of a 100-nm GaN layer, a 600-nm Al_{0.02}Ga_{0.98}N layer, a 60-nm In_{0.02}Ga_{0.98}N layer, and a 5-nm In_{0.14}Ga_{0.86}N cap layer, which are all doped with magnesium. The QW thickness is either 10.4 nm or 25 nm. The rest of the structure is the same between both device types. The ridge waveguide is 3 μm wide to ensure lateral single mode operation. The cavity length is 1 mm. The cw threshold currents are 82 mA for the laser diode with 10.4-nm-wide QW and 125 mA for the 25-nm-wide QW.

APPENDIX B: EXPERIMENTAL SETUP

The laser diodes are packaged in TO56 cans and mounted in an actively temperature stabilized heatsink. The diode is driven using a pulse generator (Stanford Research Systems

DG645) in pulses of 80 ns with a repetition rate of 20 kHz. The beam is collimated with an aspheric lens with 8 mm focal length and a second achromatic lens with 75 mm focal length is used to focus the beam into the entrance slit of the monochromator (Princeton Instruments Acton SP2300) that is connected to the streak camera (Hamamatsu C10910). For measurements at low intensity, we use photon counting with typically 480 000 exposures. The photon counting signal is processed with a Gaussian filter for better visibility in Fig. 3. For higher intensity, the images are analog integrated over 200 frames. The images are taken with a CMOS camera (Hamamatsu ORCA Flash 4.0 V2) using exposure times of 100 ms for analog integration and 10 ms for photon counting. To determine the current density, the peak voltage across the device is measured using a Tektronics DPO 7104 sampling oscilloscope. The corresponding current is determined from U-I characteristics measured in continuous wave mode. The measured current can be slightly below the real value during pulsed operation due to the different self-heating conditions in continuous wave and pulsed modes, but at the low currents that we use, this difference is not significant.

APPENDIX C: SIMULATION MODEL

The first step is to obtain the electric potential $\Phi(z)$ across the QW and barrier layers, where z is the coordinate perpendicular to the QW plane, which is also the *c* axis of the crystal. The Poisson equation includes contributions from spontaneous polarization $E_{sp}(z)$, piezoelectric polarization $E_{pz}(z)$, and the field originating from the charge density distribution $E_{\rho}(z) = \int_{-\infty}^z \rho(z') dz'$:

$$-\frac{\partial}{\partial z} \Phi(z) = E_{sp}(z) + E_{pz}(z) + E_{\rho}(z). \quad (C1)$$

In the experiment, the p-n junction is driven with forward bias, therefore the field arising from the p-n junction vanishes and is not taken into account in the calculations. The charge density $\rho(z)$ depends on the carrier density N and the spatial distributions $|\psi_{c,i}|^2$, $|\psi_{v,j}|^2$ of electrons and holes occupying the conduction bands *i* and valence bands *j*, respectively:

$$\rho(z) = qN \left(- \sum_i |\psi_{c,i}|^2 + \sum_j |\psi_{v,j}|^2 \right). \quad (C2)$$

The elementary charge is denoted as q . Because the wave functions depend on the potential again, it is necessary to find a self-consistent solution to the Poisson and Schrödinger equations. First, $E_{\rho}(z)$ is set to zero and the potential is calculated for the case of no charge carriers. Then the solution of the Schrödinger equation (as described below) gives the wave functions of electrons and holes and, with these, the potential can be calculated again using Eqs. (C2) and (C1). Using the updated potential, new wave functions can be determined and this loop is repeated until the solutions converge.

The total potentials for conduction/valence bands $V_{v/c}(z) = \Phi(z) + V_{v/c}^{QW}$ are calculated from adding a rectangular QW potential $V_{v/c}^{QW}$ with the band offset ratio equal to $\Delta E_v/\Delta E_c = 0.2/0.8$ [33]. The Schrödinger equations for

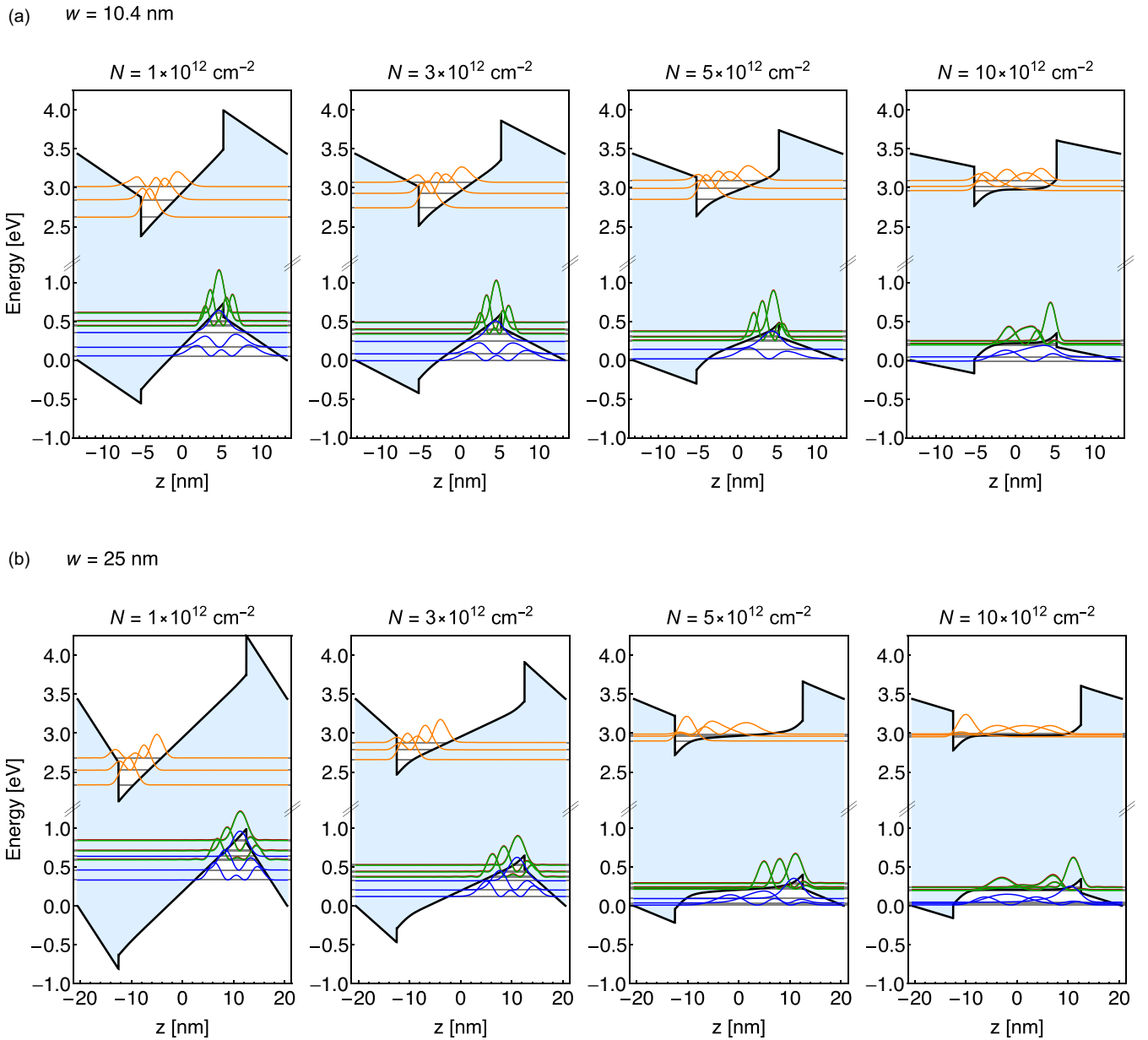


FIG. 8. Potential, squared absolute wave functions and energy states for conduction and valence bands in (a) 10.4-nm and (b) 25-nm-wide QWs, shown for different charge carrier densities N . The orange lines show conduction band electron wave functions, whereas the heavy hole, light hole, and crystal-field split-off states are drawn in red, green, and blue, respectively. For clarity, only the three lowest states of each type are shown. Heavy- and light-hole wave functions are almost identical (green lines hide red lines), whereas the split-off states are barely involved in recombination.

conduction and valence bands can be written as

$$\left[\mathcal{H}_c \left(\frac{\partial}{\partial z} \right) + V_c(z) \right] \vec{\psi}_{c,i}(z) = E_{c,i} \vec{\psi}_{c,i}(z), \quad (\text{C3})$$

$$\left[\mathcal{H}_v \left(\frac{\partial}{\partial z} \right) + V_v(z) \right] \psi_{v,j}(z) = E_{v,j} \psi_{v,j}(z). \quad (\text{C4})$$

Based on the $k \cdot p$ theory, a 6×6 Hamiltonian is used for the valence band. The six basis states are $|U_1\rangle = -\frac{1}{\sqrt{2}}(|P_x \uparrow\rangle + i|P_y \uparrow\rangle)$, $|U_2\rangle = \frac{1}{\sqrt{2}}(|P_x \uparrow\rangle - i|P_y \uparrow\rangle)$, $|U_3\rangle = |P_z \uparrow\rangle$, $|U_4\rangle = \frac{1}{\sqrt{2}}(|P_x \downarrow\rangle - i|P_y \downarrow\rangle)$, $|U_5\rangle = -\frac{1}{\sqrt{2}}(|P_x \downarrow\rangle +$

$i|P_y \downarrow\rangle)$, $|U_6\rangle = |P_z \downarrow\rangle$. This basis forms the vector $\vec{\psi}_{c,i}$. The s -like conduction band uses only the two basis states $|S \uparrow\rangle$ and $|S \downarrow\rangle$, which are practically treated as spin degenerate anyway. Further details of this model as well as the explicit Hamiltonians were described by Scheibenzuber *et al.* [33]. The same effective mass parameters are used for the whole structure consisting of QWs and barriers. After Fourier transformation of the potential and series expansion of the eigenfunctions, the equations can be solved as matrix eigenvalue problems. We get the energies and wave functions for each conduction band and valence band state (including heavy hole, light hole, and crystal-field split-off bands), in dependence on the in-plane

wave vector (e.g., k_x) or, in other words, the complete band structure in the vicinity of the Γ point.

To obtain the population of each band, the quasi-Fermi levels μ_c and μ_v for each given carrier density N need to be determined, which is done via the following equations:

$$N = \sum_i \frac{1}{2\pi} \int_0^\infty f_c[E_{c,i}(k_x)] k_x dk_x \quad (\text{C5})$$

$$N = \sum_j \frac{1}{2\pi} \int_0^\infty (1 - f_v[E_{v,j}(k_x)]) k_x dk_x \quad (\text{C6})$$

using the Fermi-Dirac distribution that includes the Boltzmann constant k_B and temperature T :

$$f_{v/c}(E) = \left[1 + \exp\left(\frac{E - \mu_{v/c}}{k_B T}\right) \right]^{-1}. \quad (\text{C7})$$

Now we can calculate the momentum matrix elements $M_{ij}(k_x)$ for different polarization directions and the rate of spontaneous emission $r(\hbar\omega)$ as a function of photon energy $\hbar\omega$:

$$\begin{aligned} |M_{ij}^\perp(k_x)|^2 &= |\langle S | p_x | P_x \rangle|^2 |\langle \psi_{c,i} | \psi_{v,j} \rangle|^2 \\ &= \frac{1}{2} E_p^\perp m_0 |\langle \psi_{c,i} | \psi_{v,j} \rangle|^2, \end{aligned} \quad (\text{C8})$$

$$\begin{aligned} |M_{ij}^\parallel(k_x)|^2 &= |\langle S | p_z | P_z \rangle|^2 |\langle \psi_{c,i} | \psi_{v,j} \rangle|^2 \\ &= \frac{1}{2} E_p^\parallel m_0 |\langle \psi_{c,i} | \psi_{v,j} \rangle|^2, \end{aligned} \quad (\text{C9})$$

$$\begin{aligned} r(\hbar\omega) &= \frac{q^2 n_{\text{eff}} \omega}{2\pi^3 d \hbar m_0^2 c^3 \varepsilon_0 E_{\text{hom}}} \sum_{i,j} \int_0^\infty |M_{ij}(k_x)|^2 \\ &\times f_c(E_{c,i}(k_x)) [1 - f_v(E_{v,j}(k_x))] \\ &\times \text{sech}\left(\frac{E_{c,i}(k_x) - E_{v,j}(k_x) - \hbar\omega}{E_{\text{hom}}}\right) k_x dk_x. \end{aligned} \quad (\text{C10})$$

In Eq. (C10), either $|M_{ij}^\perp(k_x)|^2$ for TE or $|M_{ij}^\parallel(k_x)|^2$ for TM polarization can be inserted. Using the sum of both squared matrix elements gives the total emission rate including all polarization directions. In these equations, we use the momentum operators p_x and p_z , the momentum matrix element energy E_p , the electron mass m_0 , the effective refractive index n_{eff} , angular frequency ω , reduced Planck's constant \hbar , the QW thickness d , the speed of light in vacuum c , the dielectric constant ε_0 , and the homogeneous linewidth energy $E_{\text{hom}} = 25 \text{ meV}$.

APPENDIX D: QW POTENTIAL AND ELECTRONIC STATES

Figure 8 shows the carrier-density-dependent behavior of the QW potential and few electronic states for a 10.4-nm and 25-nm-wide QW. Between a carrier density of 10^{12} cm^{-2} and 10^{13} cm^{-2} , the potential is strongly deformed from a triangular towards a rectangular well. However, there are still sharp dips at the edges of the QW, even in the case of $N = 10^{13} \text{ cm}^{-2}$, where the screening effect has mostly saturated. The ground states of electrons and holes are localized in these dips and, in this way, they are mainly responsible for screening the polarization field. A certain degree of asymmetry in the charge distribution (and thus in the potential shape) is necessary to obtain a screening effect.

The general effects are similar in 10.4-nm and 25-nm-wide QWs, but the transition between quantum confinement and the bulklike state is more abrupt for the wider QW, as shown, e.g., in Fig. 5. For the 25-nm-wide QW, the potential remains almost constant for carrier densities above $5 \times 10^{12} \text{ cm}^{-2}$. The crystal-field split-off states are several 100 meV apart from the respective heavy hole and light hole states, thus they are negligibly populated and sometimes poorly confined if the carrier density becomes high.

- [1] L. A. Coldren, S. W. Corzine, and M. L. Mashanovitch, *Diode Lasers and Photonic Integrated Circuits* (John Wiley & Sons, Inc., Hoboken, New Jersey, USA, 2012).
- [2] *III-Nitride Based Light Emitting Diodes and Applications*, edited by T.-Y. Seong, J. Han, H. Amano, and H. Morkoc (Springer, Dordrecht, Netherlands, 2013).
- [3] D. A. B. Miller, Optical physics of quantum wells, in *Quantum Dynamics of Simple Systems* (CRC Press, Boca Raton, Florida, USA, 2020), pp. 239–266.
- [4] U. T. Schwarz, Physics and technology of AlGaInN-based laser diode, in *Encyclopedia of Applied Physics* (Wiley-VCH Verlag GmbH & Co. KGaA, Weinheim, Germany, 2021), pp. 1–32.
- [5] S. F. Chichibu, A. C. Abare, M. S. Minsky, S. Keller, S. B. Fleischer, J. E. Bowers, E. Hu, U. K. Mishra, L. A. Coldren, S. P. DenBaars, and T. Sota, Effective band gap inhomogeneity and piezoelectric field in InGaInN/GaN multiquantum well structures, *Appl. Phys. Lett.* **73**, 2006 (1998).
- [6] H. S. Kim, J. Y. Lin, H. X. Jiang, W. W. Chow, A. Botchkarev, and H. Morkoc, Piezoelectric effects on the optical properties

of GaN/Al_xGa_{1-x}N multiple quantum wells, *Appl. Phys. Lett.* **73**, 3426 (1998).

- [7] T. Takeuchi, S. Sota, M. Katsuragawa, M. Komori, H. Takeuchi, H. Amano, and I. Akasaki, Quantum-confined Stark effect due to piezoelectric fields in GaInN strained quantum wells, *Jpn. J. Appl. Phys.* **36**, L382 (1997).
- [8] T. Takeuchi, C. Wetzel, S. Yamaguchi, H. Sakai, H. Amano, I. Akasaki, Y. Kaneko, S. Nakagawa, Y. Yamaoka, and N. Yamada, Determination of piezoelectric fields in strained GaInN quantum wells using the quantum-confined Stark effect, *Appl. Phys. Lett.* **73**, 1691 (1998).
- [9] M. Leroux, N. Grandjean, M. Lüty, J. Massies, B. Gil, P. Lefebvre, and P. Bigenwald, Quantum confined Stark effect due to built-in internal polarization fields in (Al,Ga)N/GaN quantum wells, *Phys. Rev. B* **58**, R13371(R) (1998).
- [10] F. D. Sala, A. D. Carlo, P. Lugli, F. Bernardini, V. Fiorentini, R. Scholz, and J.-M. Jancu, Free-carrier screening of polarization fields in wurtzite GaN/InGaIn laser structures, *Appl. Phys. Lett.* **74**, 2002 (1999).

- [11] L.-H. Peng, C.-W. Chuang, and L.-H. Lou, Piezoelectric effects in the optical properties of strained InGaN quantum wells, *Appl. Phys. Lett.* **74**, 795 (1999).
- [12] J. Bai, T. Wang, and S. Sakai, Influence of the quantum-well thickness on the radiative recombination of InGaN/GaN quantum well structures, *J. Appl. Phys.* **88**, 4729 (2000).
- [13] T. Świetlik, G. Franssen, P. Wiśniewski, S. Krukowski, S. P. Łepkowski, L. Marona, M. Leszczyński, P. Prystawko, I. Grzegory, T. Suski, S. Porowski, P. Perlin, R. Czernecki, A. Bering-Staniszevska, and P. G. Eliseev, Anomalous temperature characteristics of single wide quantum well InGaN laser diode, *Appl. Phys. Lett.* **88**, 071121 (2006).
- [14] N. F. Gardner, G. O. Müller, Y. C. Shen, G. Chen, S. Watanabe, W. Götz, and M. R. Krames, Blue-emitting InGaN–GaN double-heterostructure light-emitting diodes reaching maximum quantum efficiency above 200 A/cm², *Appl. Phys. Lett.* **91**, 243506 (2007).
- [15] A. Laubsch, W. Bergbauer, M. Sabathil, M. Strassburg, H. Lugauer, M. Peter, T. Meyer, G. Brüderl, J. Wagner, N. Linder, K. Streubel, and B. Hahn, Luminescence properties of thick InGaN quantum-wells, *Phys. Status Solidi C* **6**, S885 (2009).
- [16] G. Muziol, M. Hajdel, M. Siekacz, K. Szkudlarek, S. Stanczyk, H. Turski, and C. Skierbiszewski, Optical properties of III-nitride laser diodes with wide InGaN quantum wells, *Appl. Phys. Express* **12**, 072003 (2019).
- [17] G. Muziol, H. Turski, M. Siekacz, K. Szkudlarek, L. Janicki, M. Baranowski, S. Zolud, R. Kudrawiec, T. Suski, and C. Skierbiszewski, Beyond quantum efficiency limitations originating from the piezoelectric polarization in light-emitting devices, *ACS Photonics* **6**, 1963 (2019).
- [18] A. Bercha, W. Trzeciakowski, G. Muziol, M. Siekacz, and C. Skierbiszewski, Anomalous photocurrent in wide InGaN quantum wells, *Opt. Express* **28**, 4717 (2020).
- [19] K. Pieniak, W. Trzeciakowski, G. Muziol, A. Kafar, M. Siekacz, C. Skierbiszewski, and T. Suski, Evolution of a dominant light emission mechanism induced by changes of the quantum well width in InGaN/GaN LEDs and LDs, *Opt. Express* **29**, 40804 (2021).
- [20] G. Muziol, M. Hajdel, M. Siekacz, H. Turski, K. Pieniak, A. Bercha, W. Trzeciakowski, R. Kudrawiec, T. Suski, and C. Skierbiszewski, III-nitride optoelectronic devices containing wide quantum wells—unexpectedly efficient light sources, *Jpn. J. Appl. Phys.* **61**, SA0801 (2022).
- [21] M. Hajdel, M. Chlipała, M. Siekacz, H. Turski, P. Wolny, K. Nowakowski-Szkudlarek, A. Feduniewicz-Żmuda, C. Skierbiszewski, and G. Muziol, Dependence of InGaN quantum well thickness on the nature of optical transitions in LEDs, *Materials* **15**, 237 (2021).
- [22] J. W. Tomm, A. Bercha, G. Muziol, J. Piprek, and W. Trzeciakowski, Recombination in polar InGaN/GaN LED structures with wide quantum wells, *Phys. Status Solidi RRL* **2300027** (2023).
- [23] S. Schmitt-Rink, D. Chemla, and D. Miller, Linear and non-linear optical properties of semiconductor quantum wells, *Adv. Phys.* **38**, 89 (1989).
- [24] R. Dingle, W. Wiegmann, and C. H. Henry, Quantum States of Confined Carriers in Very thin Al_xGa_{1-x}As–GaAs–Al_xGa_{1-x}As Heterostructures, *Phys. Rev. Lett.* **33**, 827 (1974).
- [25] L. L. Chang, L. Esaki, and R. Tsu, Resonant tunneling in semiconductor double barriers, *Appl. Phys. Lett.* **24**, 593 (1974).
- [26] O. Ambacher, D. Brunner, R. Dimitrov, M. Stutzmann, A. Sohmer, and F. Scholz, Absorption of InGaN single quantum wells determined by photothermal deflection spectroscopy, *Jpn. J. Appl. Phys.* **37**, 745 (1998).
- [27] C. Skierbiszewski, H. Turski, G. Muziol, M. Siekacz, M. Sawicka, G. Cywiński, Z. R. Wasilewski, and S. Porowski, Nitride-based laser diodes grown by plasma-assisted molecular beam epitaxy, *J. Phys. D* **47**, 073001 (2014).
- [28] L. Uhlig, M. Wachs, D. J. Kunzmann, and U. T. Schwarz, Spectral-temporal dynamics of (Al,In)GaN laser diodes, *Opt. Express* **28**, 1771 (2020).
- [29] A. David, C. A. Hurni, N. G. Young, and M. D. Craven, Field-assisted shockley-read-hall recombinations in III-nitride quantum wells, *Appl. Phys. Lett.* **111**, 233501 (2017).
- [30] A. Bercha, W. Trzeciakowski, G. Muziol, J. W. Tomm, and T. Suski, Evidence for “dark charge” from photoluminescence measurements in wide InGaN quantum wells, *Opt. Express* **31**, 3227 (2023).
- [31] S. Chuang, Optical gain of strained wurtzite GaN quantum-well lasers, *IEEE J. Quantum Electron.* **32**, 1791 (1996).
- [32] W. W. Chow and S. W. Koch, *Semiconductor-Laser Fundamentals* (Springer, Berlin, 1999).
- [33] W. G. Scheibenzuber, U. T. Schwarz, R. G. Veprek, B. Witzigmann, and A. Hangleiter, Calculation of optical eigenmodes and gain in semipolar and nonpolar InGaN/GaN laser diodes, *Phys. Rev. B* **80**, 115320 (2009).
- [34] I. Vurgaftman and J. R. Meyer, Electron bandstructure parameters, in *Nitride Semiconductor Devices: Principles and Simulation* (Wiley-VCH Verlag GmbH & Co. KGaA, Weinheim, Germany, 2007), pp. 13–48.
- [35] K. Kojima, U. T. Schwarz, M. Funato, Y. Kawakami, S. Nagahama, and T. Mukai, Optical gain spectra for near UV to aquamarine (Al,In)GaN laser diodes, *Opt. Express* **15**, 7730 (2007).